NANO LETTERS

pubs.acs.org/NanoLett Letter

Ultrafast Laser-Engineered Hierarchical Interface for Synergistic Radiative Cooling and Droplet Energy Harvesting

Chao Chen,* Jianhan Wang, Kai Shi, Hongwen Zhang,* Peijun Lin, Xiaodong Yang,* and Dong Wu*

Cite This: https://doi.org/10.1021/acs.nanolett.6c03624 Read Online

ACCESS | Metrics & More | Article Recommendations | Supporting Information

ABSTRACT: Passive daytime radiative cooling provides an energy-free approach for thermal management, but achieving multifunctional operation under realistic outdoor conditions remains challenging, because optical regulation, surface wetting, and energy conversion are typically realized with separate material components. Here, we develop a femtosecond laser-engineered passive radiative cooler (FLA-PRC) based on a hierarchical PTFE/Ag/SiO_2 interface that simultaneously regulates photons, water droplets, and interfacial charges. Orthogonal laser scanning creates periodic flat-topped micropyramid arrays decorated with secondary micro/nanostructures, enabling synergistic control of solar scattering, infrared emission, and superhydrophobicity. Combined spectral measurements and FDTD simulations reveal that the laser-induced hierarchical morphology enhances solar light redistribution through multiscale scattering while promoting mid-infrared coupling and emission through increased optical interaction pathways. The Ag layer further integrates broadband solar reflection with electrostatic induction for droplet energy harvesting. This work establishes a deterministic laser-fabricated interface strategy for coordinating photonic, wetting, and electrical functions within a single-surface architecture.

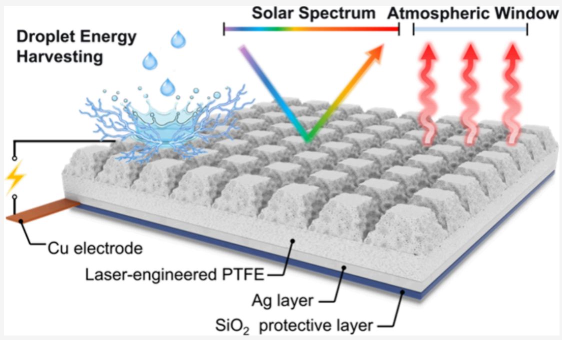

KEYWORDS: *Femtosecond laser ablation, superhydrophobic hierarchical surface, passive radiative cooling, water energy harvesting, energy-saving buildings*

Passive daytime radiative cooling (PDRC) has emerged as an energy-free thermal-management strategy by exploiting the atmospheric transparency window to dissipate heat into outer space while minimizing solar absorption.[1−5] Raman et al. experimentally demonstrated sub-ambient daytime cooling using a nanophotonic structure, establishing PDRC as a practical thermal-management strategy.[7] Diverse PDRC platforms, including nanophotonic structures, porous polymers, composites, and inorganic coatings, have been developed to enhance solar reflection and infrared emission.[6,8−22] Nanophotonic and directional cooling architectures enable precise spectral manipulation but often require sophisticated optical design and complex fabrication processes.[6,8] Porous polymers enhance scattering through air/polymer interfaces but depend strongly on pore morphology and structural stability.[9−14] Composite coatings improve optical performance and durability but often involve fillers, compatibility issues, or multistep fabrication.[15−22] Recent advances in ultrathin, self-assembled, and thermally conductive cooling films have further expanded the design space of PDRC materials for practical applications.[23,24]

Despite these advances, achieving long-term outdoor operation requires more than efficient radiative heat exchange. Dust accumulation, water retention, mechanical degradation, and environmental aging can significantly deteriorate optical performance, while many cooling systems still rely on separate functional layers or external components to achieve additional functions.[6−24] To address these challenges, multifunctional PDRC systems integrating self-cleaning, adaptive regulation, and energy harvesting have recently been attracting increased attention. Superhydrophobic coatings and Janus structures have introduced water repellency and contamination resistance into cooling surfaces.[25−27] PTFE-based porous materials and triboelectric systems have further demonstrated the possibility of coupling radiative cooling with droplet-induced electricity generation.[28,29] Adaptive photonic, phase-change, electrochromic, and humidity-responsive systems further enable dynamic thermal regulation.[30−41] Recent advances have further extended radiative thermal management toward dynamic and all-season operation. Jung et al. used laser-induced pyrolysis of PDMS to realize radiative-cooling and solar-heating states within a single material, achieving a solar reflectance of 94.6% and thermal emissivity of 99.2% in the cooling state, together with approximately 94% solar absorption in the heating state.[42]

Received: July 23, 2026
Revised: September 4, 2026
Accepted: September 4, 2026

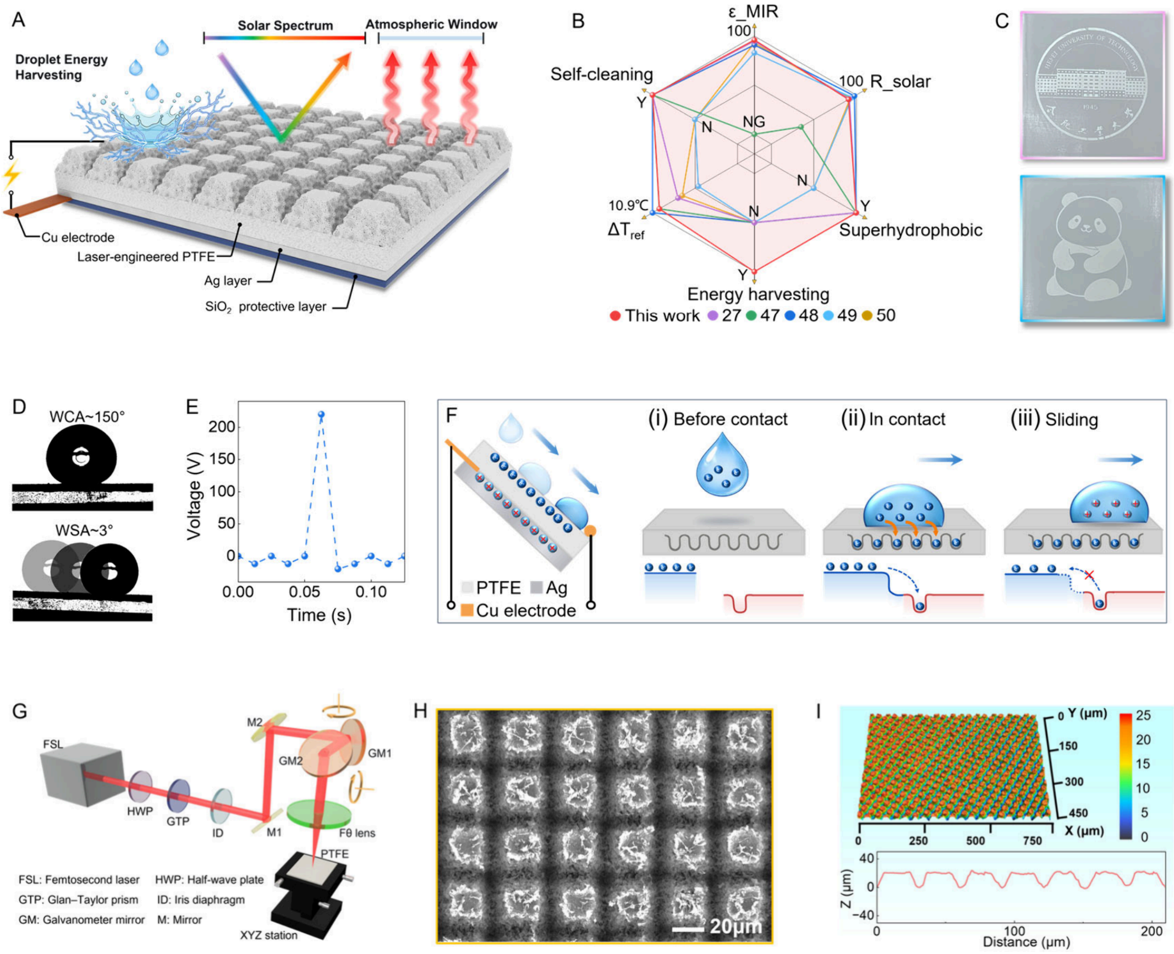

Figure 1. Concept and facile fabrication of multifunctional FLA-PRC. (A) Schematic of the FLA-PRC with integrated radiative cooling, self-cleaning, and droplet energy-harvesting functions. (B) Comparison of the multifunctional performance of FLA-PRC with previously reported passive radiative coolers. ΔT_{ref} denotes the temperature reduction relative to a blank/uncovered reference. NG indicates that the corresponding quantitative value was not reported in the original study. (C) Programmable femtosecond-laser patterning. (D) Water contact and sliding angles. (E) Droplet-induced pulsed voltage. (F) Charge-transfer and electrostatic-induction mechanism during droplet sliding. (G) Schematic of the laser fabrication process. (H) SEM images of laser-processed PTFE with flat-topped micro-pyramid arrays (scale bars = 20 μm). (I) Confocal image and height profile.

Jin et al. developed an electrochemically driven device based on reversible metal electrodeposition, enabling in situ switching between solar heating and daytime radiative cooling with a large solar absorptance modulation contrast of 0.82.[43] Liu et al. integrated a Janus aerogel with phase-change materials to achieve weather-adaptive cooling/heating regulation, demonstrating a maximum subambient cooling of 14.2 °C and a temperature rise of 14.9 °C in the respective operating modes.[44] These studies highlight the rapid development of radiative thermal management from static cooling toward adaptive and all-season thermal regulation. However, these strategies generally realize optical management, liquid control, and electrical conversion through independent material components or complex architectures. A unified interface capable of simultaneously regulating photons, water, and charge remains highly desirable for next-generation multifunctional outdoor surfaces.

Here, we report a femtosecond-laser-engineered PTFE/Ag/SiO_2 membrane (FLA-PRC) that integrates passive radiative cooling, superhydrophobic self-cleaning, and droplet energy harvesting within a single laser-defined interface. Femtosecond laser scanning directly constructs ordered flat-topped micro-pyramid arrays on PTFE without masks, templates, fillers, or chemical etching. The resulting hierarchical fluoropolymer interface provides coupled control over solar scattering, mid-infrared radiation out-coupling, air trapping, and droplet contact−separation. A backside Ag layer simultaneously serves as a broadband solar reflector and an electrostatic induction electrode, while a thin SiO_2 coating protects the metal layer during outdoor operation. By combining optical measurements with simulations, this work reveals the structure−function relationship of laser-generated micro/nanostructures for integrated outdoor thermal and energy management.

Inspired by the light-management function of Saharan silver-ant hairs,[45] orthogonal femtosecond-laser scanning directly writes periodic flat-topped micro-pyramids without masks, templates, particle fillers, or chemical etching (Figure 1A−G). PTFE was selected because its C−F bonds provide intrinsic mid-infrared absorption, while its low surface energy, chemical stability, and triboelectric tendency support water repellency and contact electrification.[46,47] The Ag backing has two roles: it returns transmitted solar radiation to the structured polymer and acts as the electrostatic induction electrode beneath the PTFE dielectric. The thin SiO_2 layer protects Ag during

https://doi.org/10.1021/acs.nanolett.6c03624
Nano Lett. XXXX, XXX, XXX−XXX

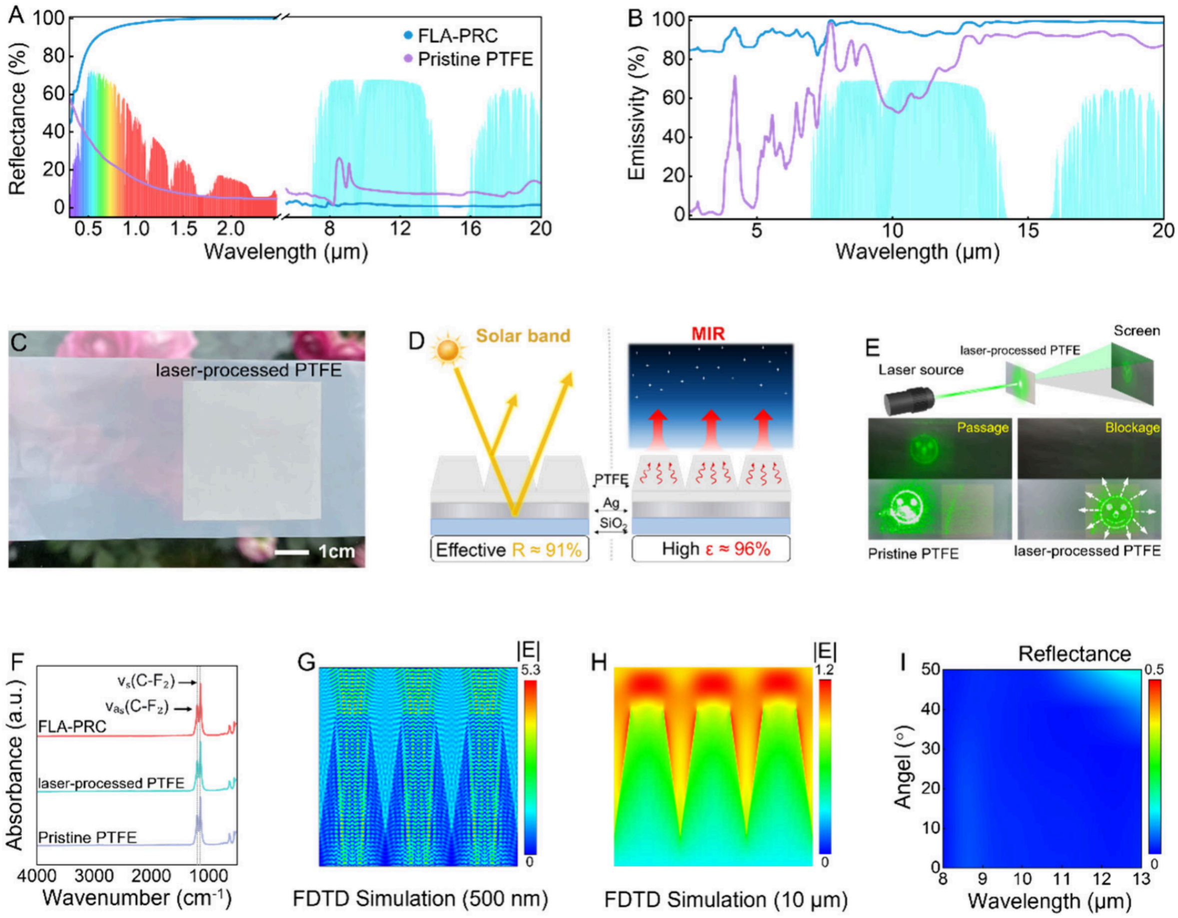

Figure 2. Study of structure−photon interaction across dual-band spectrum. (A) Reflectance spectra of pristine PTFE and FLA-PRC from 0.3 to 20 μm. (B) Mid-infrared emissivity calculated using Kirchhoff's law. (C) Partially laser-processed PTFE showing the transition from semitransparent to white and opaque. (D) Optical-regulation mechanism. (E) Laser-pointer demonstration of diffuse scattering. (F) FTIR spectra of pristine PTFE, laser-processed PTFE, and FLA-PRC. FDTD-simulated electric-field distributions at (G) 0.5 μm and (H) 10 μm. (I) FDTD-simulated angular reflectance within the 8−13 μm atmospheric window.

environmental exposure. Consequently, the same interface enables solar scattering, IR emission, air trapping, droplet shedding, and charge separation. The low sliding angle and pulsed voltage shown in Figure 1D,E preview these coupled wetting and electrical responses. Unlike previously reported laser-processed PTFE coolers that primarily exploit surface morphology for optical regulation and water repellency, FLA-PRC further couples droplet electricity generation to the same interface through the dual-function Ag layer. Figure 1B therefore compares the breadth of integrated functions rather than claiming superiority in every individual performance metric.[27,47−50] Because the optical, wetting, and electrical processes share the same front morphology, changing the laser geometry can in principle tune several responses simultaneously, making the structure−property relationship central to the device rather than incidental to fabrication.

Figure 1G schematically illustrates the deterministic femtosecond-laser fabrication strategy used to construct the hierarchical PTFE surface. Orthogonal laser scanning generates ordered flat-topped micro-pyramid arrays through controlled ablation. This deterministic pathway differs from stochastic pore formation or particle aggregation and allows the surface geometry to be programmed directly by the laser scan trajectory. The complete fabrication sequence of FLA-PRC, including orthogonal laser processing, backside Ag deposition, Cu-electrode connection, and SiO_2 encapsulation, is provided in Figure S1. SEM and confocal microscopy further characterize the resulting surface geometry, revealing a top width of approximately 20 μm, a bottom width and period of approximately 30 μm, and a height of approximately 20 μm (Figure 1H,I). Compared with the relatively smooth pristine PTFE surface (Figure S5A), the laser-processed PTFE exhibits abundant secondary micro/nanostructures, including coral-like asperities ranging from several hundred nanometers to several micrometers on the flat tops and inclined sidewalls (Figure S5B), generating pronounced hierarchical roughness. The primary geometry regulates optical scattering and air trapping, while secondary roughness enhances diffuse scattering and reduces solid−liquid contact. EDS analysis further confirms that laser processing does not introduce significant elemental changes, with pristine and laser-processed PTFE exhibiting similar C, F, and O compositions (Figure S3). Together with the FTIR analysis below, this result indicates that the altered optical and wetting behavior is governed mainly by morphology rather than detectable chemical restructuring. Programmable patterns and an 8×8 cm membrane (from four 4×4 cm units) demonstrate scalability (Figure 1C, Figure S2).

The hierarchical PTFE/Ag architecture simultaneously regulates solar input and thermal-radiation output (Figure 2). Weighted integration of the measured spectra gives an average

https://doi.org/10.1021/acs.nanolett.6c03624
Nano Lett. XXXX, XXX, XXX−XXX

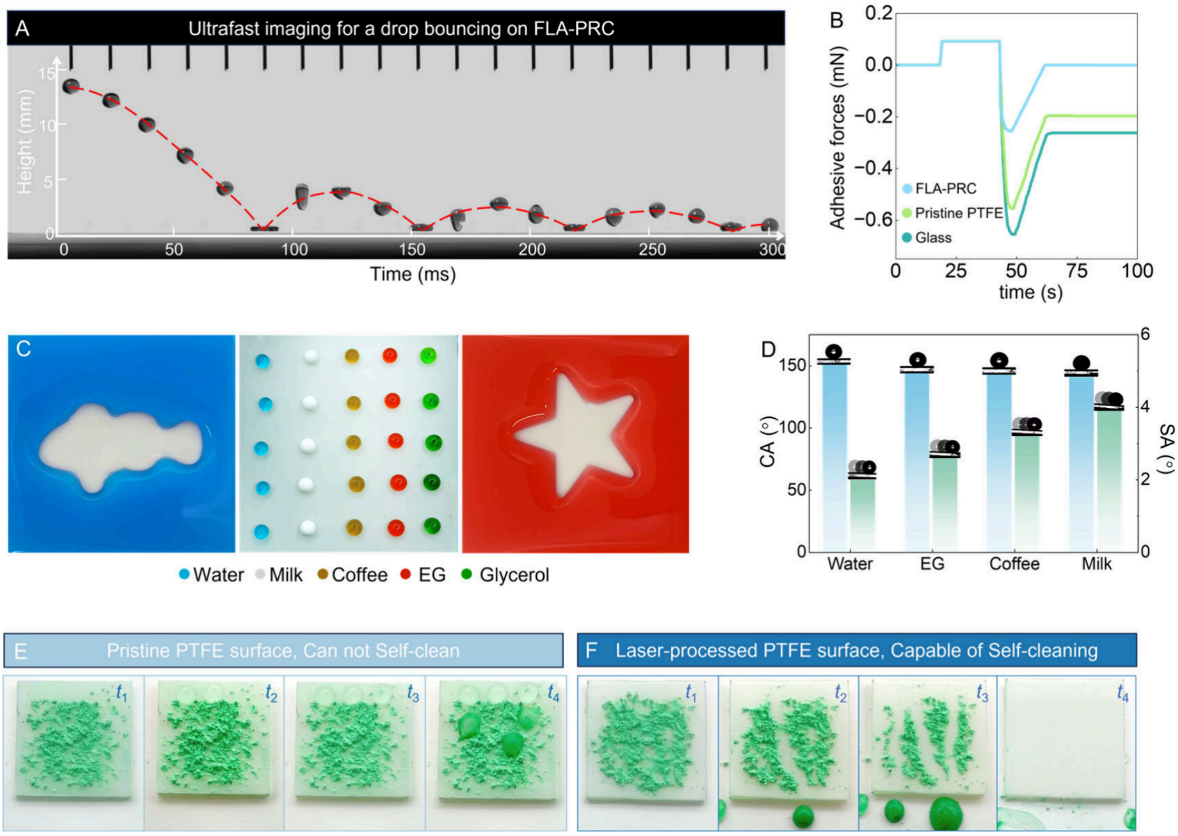

Figure 3. Hydrodynamics of diverse drops on FLA-PRC surface. (A) High-speed images of droplet impact and pancake-like rebound. (B) Adhesion-force comparison. (C) Repellency toward different liquids and spatially patterned dyed water. (D) Contact and sliding angles. (E, F) Removal of chalk dust by simulated rainwater.

solar reflectance of 24% for pristine PTFE and 91% for FLA-PRC over 0.3−2.5 μm, while the average emissivity in the 8−13 μm atmospheric window increases from 71% to 96% (Figure 2A,B). Laser processing alone raises the solar reflectance to 37% (Figure S4A), confirming that the textured polymer contributes to optical whitening but is insufficient to suppress solar transmission. The mid-infrared emissivity comparison further indicates that both the hierarchical surface morphology and Ag backing contribute to the enhanced atmospheric-window emission, with the laser-induced morphology playing the dominant role (Figure S4B). The Ag backing provides an additional enhancement by reflecting unabsorbed mid-infrared radiation back into the PTFE layer, thereby increasing the effective optical path for absorption. This division of function explains why the complete membrane combines a high solar reflectance with strong thermal emission. The transition from semitransparent pristine PTFE to a white and opaque processed region, together with the blurred green-laser image, directly visualizes the change from predominantly transmitted light to broadband diffuse scattering (Figure 2C,E). The measured 91% reflectance is produced by this cooperative architecture rather than by PTFE texture or Ag alone; the control comparison is important because it prevents the optical gain from being assigned solely to laser-induced roughness.

The solar and mid-infrared responses arise from related structural features but different wavelength-scale interactions. At solar wavelengths, the flat tops and inclined facets redirect incident light, while the secondary protrusions randomize propagation and suppress a specular transmission pathway. Light that enters the 100 μm PTFE layer is reflected by the 150 nm Ag backing and traverses the scattering region again, producing a combined scattering/back-reflection mechanism that reduces solar heat gain (Figure 2D). In the mid-infrared, the hierarchical air/PTFE interface reduces the abrupt refractive-index transition relative to a smooth film. The inclined sidewalls and rough texture introduce multiple reflection and scattering paths, extending the effective interaction length inside PTFE and increasing coupling to intrinsic C−F vibrational absorption. The Ag backing reflects unabsorbed infrared radiation back into the polymer, enabling secondary interaction rather than transmission. Because the PTFE/Ag membrane is optically opaque in this region, its absorptance is approximately 1 − R; according to Kirchhoff's law, the reduced mid-infrared reflectance therefore corresponds directly to enhanced emissivity (Figure S6). Importantly, Ag does not simply improve solar reflection at the expense of emission, because the infrared-active PTFE remains on the radiation-facing side and absorbs the field before it reaches or after it is returned by the metal reflector.

FTIR spectra provide evidence that this enhancement is structural rather than chemical. Pristine PTFE, laser-processed PTFE, and complete FLA-PRC retain the characteristic CF_2 stretching bands near 1200 and 1145 cm^{-1} and the fingerprint-region features near 640/620 and 550/500 cm^{-1}, without noticeable shifts or new bands between 4000 and 1400 cm^{-1} (Figure 2F). Laser processing and subsequent Ag/SiO_2 deposition therefore do not introduce detectable oxygen-containing or hydrocarbon-related groups. FDTD simulations based on the measured PTFE optical constants (Figure S7)

https://doi.org/10.1021/acs.nanolett.6c03624
Nano Lett. XXXX, XXX, XXX−XXX

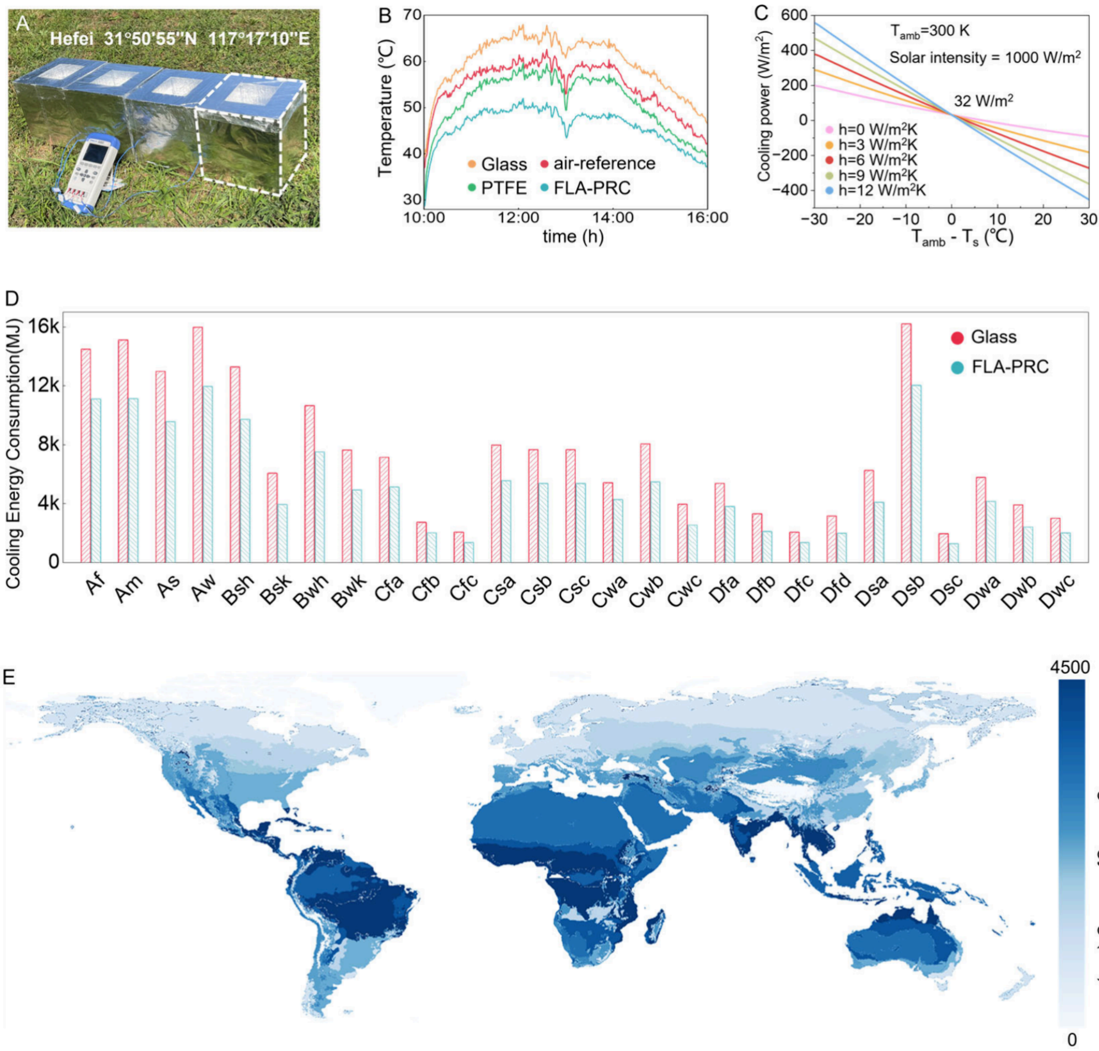

Figure 4. Theoretical calculations of cooling performance for on-site FLA-PRC. (A) Outdoor temperature-measurement setup. (B) Temperature profiles of the glass-covered, air-reference, pristine-PTFE-covered, and FLA-PRC-covered chambers under solar irradiation. (C) Calculated net cooling power as a function of temperature difference under different nonradiative heat-transfer coefficients. (D) EnergyPlus-simulated summer cooling energy consumption for glass and FLA-PRC envelopes. (E) Global distribution of projected energy-saving potential.

and the experimentally determined primary geometry further resolve the wavelength dependence. At 0.5 μm, the electric field is concentrated near the pyramid tops and is weakened along the inclined sidewalls, consistent with strong redistribution and outward scattering of incident solar radiation (Figure 2G). At 10 μm, the field couples across the entire micro-pyramid and intensifies near the sidewalls and upper region, indicating stronger infrared penetration and light−matter interaction rather than simple reflection from the surface (Figure 2H). The model captures the contribution of the periodic primary geometry, whereas the unresolved secondary roughness is expected to provide additional diffuse scattering and localized trapping. Simulated angular spectra remain at low reflectance over most incident angles in the atmospheric window, with only a modest increase at large angles and long wavelengths (Figure 2I). This angular tolerance is important because a building surface exchanges radiation with a broad sky hemisphere rather than at a single normal direction. The retention of the PTFE vibrational spectrum also excludes a competing explanation based on laser-induced oxidation. Consequently, the experimental spectra, field distributions, and angular response consistently identify geometry-mediated coupling as the dominant origin of the emission enhancement.

The same multiscale morphology establishes a low-adhesion Cassie−Baxter state (Figure S9) and protects optical performance from liquid retention and particulate contamination (Figure 3). A 10 μL water droplet released from 15 mm onto laser-processed PTFE spreads, retracts, and rebounds three times within 300 ms without evident pinning, whereas a droplet on pristine PTFE shows damped deformation and no rebound (Figure 3A, Figure S8, and Movie S1). The contrast indicates that air remains trapped beneath the droplet on the laser-processed surface, reducing real contact and energy dissipation. Water, milk, coffee, ethylene glycol, and glycerol retain nearly spherical profiles, and laser-written star and fish patterns selectively repel dyed water while the surrounding pristine region wets more strongly (Figure 3B). Thus, the wetting response originates from the locally programmed texture rather than an additional low-surface-energy coating. The water contact angle exceeds 150° and the sliding angle is approximately 3° (Figure 3C and Movie S2). Adhesion-force measurements decrease from 0.65 mN on glass and 0.55 mN on pristine PTFE to 0.25 mN on FLA-PRC (Figure 3D and

https://doi.org/10.1021/acs.nanolett.6c03624
Nano Lett. XXXX, XXX, XXX−XXX

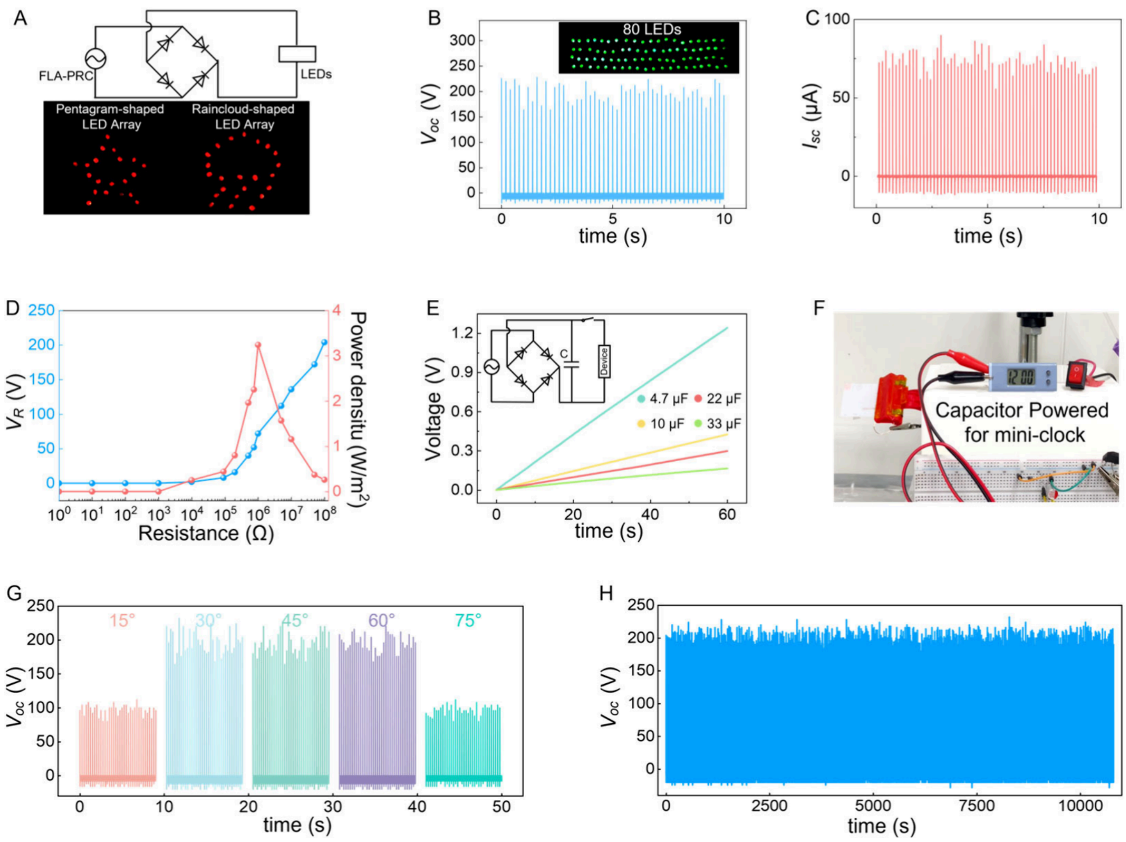

Figure 5. Droplet electricity generation relying on all-in-one FLA-PRC. (A) Intermittent illumination of LED arrays using rectified output. (B) Open-circuit voltage and (C) short-circuit current. (D) Load-dependent voltage and power density. (E) Capacitor charging after bridge rectification. (F) Timer powered by stored energy. (G) Inclination-angle-dependent voltage. (H) Output stability over 10 000 s.

Figure S10). The micro-pyramid tops restrict the contact area, while the hierarchical asperities fragment the three-phase contact line, accounting for the low retention force. Under simulated rain, chalk dust remains largely on pristine PTFE, whereas rolling droplets efficiently collect and remove the contaminants from the laser-processed FLA-PRC surface (Figure 3E,F and Movie S3), directly demonstrating the self-cleaning capability imparted by the laser-induced hierarchical morphology. This behavior is functionally linked to the other responses: rapid water shedding prevents a persistent film from modifying solar and mid-infrared transport, and fast contact–separation reduces charge neutralization during repeated droplet electricity generation. This coupling distinguishes self-cleaning from a decorative add-on: the same reduced adhesion that removes contaminants also controls the duration and reversibility of liquid contact, directly affecting both radiative exposure and electrical cycling.

Outdoor measurements translate the spectral selectivity into cooling performance (Figure 4). The samples were mounted on thermally insulated chambers that limited parasitic heat exchange while allowing the upper surface to view the sky (Figure 4A and Figure S11). Under direct solar irradiation, the FLA-PRC-covered chamber remains cooler than chambers covered by glass or pristine PTFE and reaches a maximum temperature reduction of approximately 10 °C, relative to the air-reference chamber (Figure 4B). Glass admits solar radiation and promotes internal heating, whereas pristine PTFE emits in the mid-infrared but remains partly transparent and provides weak solar scattering. FLA-PRC combines the complementary contributions identified spectroscopically: the laser-induced hierarchy redirects sunlight, Ag returns transmitted light, and the front PTFE layer retains high atmospheric-window emissivity. The temperature comparison therefore reflects simultaneous control of radiative heat input and output rather than simple shading. Although the measured temperature is influenced by weather and the chamber heat-transfer coefficient, the consistent separation among the reference surfaces supports the material-level optical interpretation. The air-reference comparison is stated explicitly because it avoids interpreting the 10 °C value as a universal subambient temperature under all climates; it represents the maximum separation measured in the specific outdoor chamber test.

A heat-balance analysis further quantifies the cooling capability by accounting for emitted thermal radiation, atmospheric back radiation, absorbed sunlight, and non-radiative convection/conduction (Figure 4C and Note S1). At an ambient temperature of 300 K, a solar irradiance of 1000 W m^{-2}, and $\Delta T = T_{amb} - T_s = 0$ K, the calculated daytime net cooling power density is approximately 32 W m^{-2}. Positive power at $\Delta T = 0$ K means that the surface has a thermodynamic driving force to cool before becoming colder than its surroundings. Under nighttime conditions at 288 K and zero solar input, the corresponding value increases to approximately 104 W m^{-2} (Figure S12), primarily because solar absorption is absent. These calculations do not replace direct calorimetry and depend on the assumed nonradiative coefficient, but they connect the measured spectrum with the expected energy balance and show why the membrane can maintain net heat rejection under both daytime and nighttime conditions.

To evaluate the building-scale consequence of this optical response, idealized EnergyPlus simulations compared envelopes assigned the measured FLA-PRC properties with conventional glass (Figure 4D,E). The building model and detailed optical, construction, and operating parameters are provided in Figure S13 and Table S1 and S3. Across the selected Köppen climate zones, the projected summer cooling-energy reduction ranges from 21.2% to 38.6%. The largest absolute saving is approximately 4180 MJ in the Temperate Continental Climate (Dsb), whereas the highest relative reduction, approximately 38.6%, occurs in the Warm Summer Continental Monsoon Climate (Dwb). The climate dependence reflects differences in incident solar load, ambient temperature, and baseline cooling demand: a location with high consumption can provide a large absolute saving, whereas a lower baseline can yield a larger percentage reduction. These simulations do not represent full-year building performance or installation economics. Instead, under the specified envelope and ideal-load assumptions, they translate the measured solar reflectance and thermal emissivity into a consistent application-level estimate of summer cooling demand (Table S2).

FLA-PRC also converts droplet motion into pulsed electrical output through contact electrification and electrostatic induction (Figure 5). When water contacts PTFE, electrons are transferred to and retained on the fluoropolymer surface. The resulting negative surface charge induces positive charge in the adjacent Ag electrode through the PTFE dielectric. As the droplet spreads, slides, and leaves the charged region, the interfacial electric field and induced charge distribution change, driving electron redistribution through the external circuit and generating alternating pulses (Figure 1F). The Ag backing thus participates in both radiative cooling and electrical conversion rather than acting as an independently attached generator. The laser-written wetting state is equally important: sufficient liquid−solid contact is required for electrification, but low adhesion and rapid separation limit residual water and preserve the charge gradient for subsequent droplets. Accordingly, the electrical output is governed by the coupled evolution of contact area, sliding velocity, and separation time rather than by surface charge alone. The contact electrode on the water-facing side completes the circuit, whereas the buried Ag layer senses the changing field without obstructing droplet motion or the radiative surface.

A falling water droplet produces an open-circuit voltage of 220 V, a short-circuit current of 89 μA, and a transferred charge of 74 nC (Figure 5B,C and Figure S14). The load-dependent response exhibits impedance matching, with an areal power density of 3.24 W m^{-2} at 1 MΩ (Figure 5D). After bridge rectification, one tap-water droplet intermittently illuminates up to 80 LEDs, while repeated pulses charge a capacitor that subsequently powers a small timer (Figure 5A,E,F and Movies S4 and S5). These demonstrations establish pulse rectification and storage rather than continuous high-power operation. The voltage rises as the falling height increases from 20 to 60 cm (Figure S15), consistent with greater gravitational input and impact deformation. Using the droplet gravitational potential energy and pulse-resolved electrical output, the conversion efficiency is estimated to be 17.9% (Note S2). The inclination dependence further reveals an interfacial optimum (Figure 5G): at a small angle, slow motion produces incomplete spatial separation of charge, whereas at a large angle the short contact time limits electrification; an intermediate angle balances contact and separation and yields the maximum voltage. Stable pulsed output over 10 000 s indicates tolerance to repeated sliding (Figure 5H). Rainfall can temporarily weaken radiative cooling by blocking sky exposure or wetting the surface, but it simultaneously supplies mechanical energy. The two functions therefore respond complementarily to weather rather than operating as unrelated demonstrations. The combination of stable cycling, load matching, and stored-energy demonstrations is more informative than the high open-circuit voltage alone, because it verifies charge transfer under repeated operation and shows how the pulsed output can be conditioned for use.

In summary, we demonstrate a femtosecond-laser-engineered PTFE/Ag/SiO_2 interface integrating radiative cooling, self-cleaning, and droplet energy harvesting within a single architecture. The laser-generated flat-topped micropyramids and secondary micro/nanostructures establish a hierarchical optical and wetting interface. By combining spectral characterization with FDTD simulations, we clarify how the laser-induced morphology regulates solar scattering, infrared optical coupling, and radiative emission. Meanwhile, the superhydrophobic interface facilitates rapid droplet motion and charge separation, while the Ag layer provides dual functions of solar reflection and electrostatic induction. These findings demonstrate that laser-defined hierarchical interfaces can couple photon management, liquid dynamics, and charge transport, offering a general strategy for multifunctional outdoor energy- and thermal-management surfaces.

■ ASSOCIATED CONTENT

Supporting Information

The Supporting Information is available free of charge at https://pubs.acs.org/doi/10.1021/acs.nanolett.6c03624.

Movie 1: bouncing dynamics of a droplet impacting on the FLA-PRC surface (MP4)

Movie 2: CCD monitoring of sliding angles of diverse liquids on the FLA-PRC (MP4)

Movie 3: self-cleaning process (MP4)

Movie 4: FLA-PRC powers 80 LEDs via a droplet (MP4)

Movie 5: FLA-PRC charges the capacitor through a rectifier bridge to power the timer (MP4)

Notes S1 and S2: calculations of radiative cooling power and energy conversion efficiency. Figures S1−S15: fabrication and characterization of FLA-PRC, optical properties, cooling mechanism, surface wettability, droplet-induced energy harvesting, outdoor cooling measurements, and building energy simulations. Tables S1−S3: optical parameters, simulated cooling-energy consumption, and building energy simulation parameters (PDF)

■ AUTHOR INFORMATION

Corresponding Authors

Chao Chen − *Department of Materials Physics and New Energy Device, School of Materials Science and Engineering, Hefei University of Technology, Hefei 230009, China;* orcid.org/0000-0002-8061-0292; Email: chaoc11@ustc.edu.cn

Hongwen Zhang − *Key Laboratory of Materials Physics, Anhui Key Laboratory of Nanomaterials and Nanotechnology, Institute of Solid State Physics, Hefei*

https://doi.org/10.1021/acs.nanolett.6c03624
Nano Lett. XXXX, XXX, XXX−XXX

Institutes of Physical Science, Chinese Academy of Sciences, Hefei 230031, P. R. China; orcid.org/0000-0002-1358-7336; Email: hwzhang@issp.ac.cn

Xiaodong Yang − *State Key Laboratory of High Efficiency and High Quality Electric Energy Conversion, Hefei University of Technology, Hefei 230009, China*; Email: xd.yang@hfut.edu.cn

Dong Wu − *Department of Precision Machinery and Precision Instrumentation, University of Science and Technology of China, Hefei 230026, China*; orcid.org/0000-0003-0623-1515; Email: dongwu@ustc.edu.cn

Authors

Jianhan Wang − *Department of Materials Physics and New Energy Device, School of Materials Science and Engineering, Hefei University of Technology, Hefei 230009, China*

Kai Shi − *Department of Materials Physics and New Energy Device, School of Materials Science and Engineering, Hefei University of Technology, Hefei 230009, China*

Peijun Lin − *Department of Materials Physics and New Energy Device, School of Materials Science and Engineering, Hefei University of Technology, Hefei 230009, China*

Complete contact information is available at: https://pubs.acs.org/10.1021/acs.nanolett.6c03624

Author Contributions

C.C. conceived the idea and supervised the overall project. **C.C.** and **D.W.** developed the methodology and device design. **J.W.** prepared and fabricated the samples, built the experimental setup, performed the experiments, and conducted the data analysis. **P.L.** and **K.S.** assisted in sample fabrication and characterization. **J.W.** and **C.C.** wrote the paper. **H.Z.** and **X.Y.** reviewed and edited the manuscript. All authors discussed the results, commented on the paper, and contributed to the writing of the manuscript.

Notes

The authors declare no competing financial interest.

■ ACKNOWLEDGMENTS

This study was supported by the National Key Research and Development Program of China (No. 2024YFB4610700) and Fundamental Research Funds for the Central Universities (Grant No. JZ2025HGTG0269), and the Natural Science Foundation of Anhui Province (Grant No. JZ2024AKZR0561), and Anhui Provincial Natural Science Foundation (Grant No. 2408085J031), and HFIPS Director's Fund (Grant No. YZJJ202402-CX).

■ REFERENCES

(1) Dong, Y.; Zhang, X.; Chen, L.; Meng, W.; Wang, C.; Cheng, Z.; Liang, H.; Wang, F. Progress in Passive Daytime Radiative Cooling: A Review from Optical Mechanism, Performance Test, and Application. *Renew. Sustain. Energy Rev.* **2023**, *188*, 113801.

(2) Liang, J.; Wu, J.; Guo, J.; Li, H.; Zhou, X.; Liang, S.; Qiu, C.-W.; Tao, G. Radiative Cooling for Passive Thermal Management towards Sustainable Carbon Neutrality. *Natl. Sci. Rev.* **2023**, *10*, nwac208.

(3) Sui, C.; Hsu, P.-C. Standardizing the Thermodynamic Definition of Daytime Subambient Radiative Cooling. *ACS Energy Lett.* **2024**, *9*, 2997−3000.

(4) Kim, H. R.; Han, W. B.; Heo, S.-Y.; Go, Y. S.; Hwang, S.-W.; Song, Y. M. Bio-Inspired Strategy for Radiation-Based Thermal Management and Utilization. *Adv. Sci.* **2025**, *12*, No. e02851.

(5) Liu, J.; Tang, H.; Jiang, C.; Wu, S.; Ye, L.; Zhao, D.; Zhou, Z. Micro-Nano Porous Structure for Efficient Daytime Radiative Sky Cooling. *Adv. Funct. Mater.* **2022**, *32*, 2206962.

(6) Lee, M.; Kim, G.; Jung, Y.; Pyun, K. R.; Lee, J.; Kim, B.-W.; Ko, S. H. Photonic Structures in Radiative Cooling. *Light Sci. Appl.* **2023**, *12*, 134.

(7) Raman, A.; Anoma, M.; Zhu, L.; et al. Passive radiative cooling below ambient air temperature under direct sunlight. *Nature.* **2014**, *515*, 540−544.

(8) Bhatia, B.; Leroy, A.; Shen, Y.; Zhao, L.; Gianello, M.; Li, D.; Gu, T.; Hu, J.; Soljačić, M.; Wang, E. N. Passive Directional Sub-Ambient Daytime Radiative Cooling. *Nat. Commun.* **2018**, *9*, 5001.

(9) Wang, T.; Wu, Y.; Shi, L.; Hu, X.; Chen, M.; Wu, L. A Structural Polymer for Highly Efficient All-Day Passive Radiative Cooling. *Nat. Commun.* **2021**, *12*, 365.

(10) Wei, L.; Li, N.; Liu, H.; Sun, C.; Chen, A.; Yang, R.; Qin, Y.; Bao, H. Macro-Nanoporous Film with Cauliflower-Shaped Fibers for Highly Efficient Passive Daytime Radiative Cooling. *ACS Appl. Mater. Interfaces* **2024**, *16*, 55609−55618.

(11) Leroy, A.; Bhatia, B.; Kelsall, C. C.; Castillejo-Cuberos, A.; Di Capua, H. M.; Zhao, L.; Zhang, L.; Guzman, A. M.; Wang, E. N. High-Performance Subambient Radiative Cooling Enabled by Optically Selective and Thermally Insulating Polyethylene Aerogel. *Sci. Adv.* **2019**, *5*, eaat9480.

(12) Feng, C.; Yang, P.; Liu, H.; Mao, M.; Liu, Y.; Xue, T.; Fu, J.; Cheng, T.; Hu, X.; Fan, H. J.; Liu, K. Bilayer Porous Polymer for Efficient Passive Building Cooling. *Nano Energy* **2021**, *85*, 105971.

(13) Wang, Y.; Wang, T.; Liang, J.; Wu, J.; Yang, M.; Pan, Y.; Hou, C.; Liu, C.; Shen, C.; Tao, G.; Liu, X. Controllable-Morphology Polymer Blend Photonic Metafoam for Radiative Cooling. *Mater. Horiz.* **2023**, *10*, 5060−5070.

(14) Shi, M.; Song, Z.; Ni, J.; Du, X.; Cao, Y.; Yang, Y.; Wang, W.; Wang, J. Dual-Mode Porous Polymeric Films with Coral-like Hierarchical Structure for All-Day Radiative Cooling and Heating. *ACS Nano* **2023**, *17*, 2029−2038.

(15) Zhang, W.; Wang, Y.; Sun, H.; Liu, C.; Shen, C.; Liu, X. Thermal Conductive High-Density Polyethylene/Boron Nitride Composites with High Solar Reflectivity for Radiative Cooling. *Adv. Compos. Hybrid Mater.* **2023**, *6*, 163.

(16) Zhu, B.; Qin, Y.; Li, M.; Zhang, Z.; Wang, Y.; Yang, R.; Xu, K.; Zhang, J.; Zhou, Y.; Guo, Y.; Wang, X.; Wu, Z.; Cai, T.; Nishimura, K.; Lin, C.-T.; Li, Y.; Jiang, N.; Li, L.; Yu, J. Thermal Conductive Radiative Cooler Enabled by Janus Structure for Above-Ambient Daytime Cooling. *Nano Energy* **2025**, *141*, 111124.

(17) Cai, C.; Chen, F.; Wei, Z.; Ding, C.; Chen, Y.; Wang, Y.; Fu, Y. Large Scalable, Anti-Ultraviolet, Strong Cellulose Film with Well-Defined Dual-Pores for Longtime Daytime Radiative Cooling. *Chem. Eng. J.* **2023**, *476*, 146668.

(18) Feng, S.; Yao, L.; Feng, M.; Cai, H.; He, X.; He, M.; Bu, X.; Zhou, Y.; Zhang, T. Sustainable Regeneration of Waste Polystyrene Foam as Cooling Coating: Building Cooling Energy Saving, CO_2 Emission Reduction and Cost-Benefit Prospective. *J. Cleaner Prod.* **2024**, *434*, 140361.

(19) Li, Y.; Yin, Y.; Bai, Y.; Dong, H.; Yang, T.; Gao, Y.; Ma, W. Engineering the Optical Properties of $SrZrO_3$ Crystals via Zn Doping for Superior Passive Daytime Radiative Cooling. *J. Adv. Ceram.* **2025**, *14*, 9221107.

(20) Li, Z.; Lin, X.; Yu, T.; Guo, Y.; He, S.; Chen, C.; Wu, Y. Biomimetic, Robust, Recyclable Radiative Cooler via Water-Triggered Multistage Self-Assembly Toward Sustainable Agriculture. *ACS Energy Lett.* **2026**, *11*, 3516−3527.

(21) Li, S.; Du, G.; Pan, M.; Wang, X.; Dong, X.; Huang, T.; Hu, D.; Ren, T.; Li, X.; Chen, H.; Mai, X. Scalable and Sustainable Hierarchical-Morphology Coatings for Passive Daytime Radiative Cooling. *Adv. Compos. Hybrid Mater.* **2024**, *7*, 15.

(22) Zhang, Q.; Xue, T.; Lu, Y.; Ma, L.; Yu, D.; Liu, T.; Fan, W. Fluorine-Containing Polyimide Nanofiber Membranes for Durable and Anti-Aging Daytime Radiative Cooling. *J. Mater. Sci. Technol.* **2024**, *179*, 166−173.

(23) Jaramillo-Fernandez, J.; Whitworth, G. L.; Pariente, J. A.; Blanco, A.; Garcia, P. D.; Lopez, C.; Sotomayor-Torres, C. M. A Self-Assembled 2D Thermofunctional Material for Radiative Cooling. *Small* **2019**, *15*, 1905290.
(24) Zhang, W.; Yan, Q.; He, W.; Tu, S.; Feng, J. A Dual Photonic Structure with Beaded Networks and Core−Shell Nanoparticles for Ultrathin yet High-Performance Passive Daytime Radiative Cooling Coatings. *ACS Appl. Mater. Interfaces* **2026**, *18*, 5967−5978.
(25) Ran, X.; Liu, C.; Chen, B. Synergistic Radiative-Evaporative Cooling Film for High-Efficiency Daytime Passive Cooling and Photovoltaic Thermal Management. *J. Mater. Sci. Technol.* **2026**, *249*, 189−195.
(26) Li, Z.; Bashir, A.; Tang, C.-Y.; Tsui, G. C.-P.; Chen, Y.; Cui, J.; Ouyang, X.; Liu, C.; Chen, D. Thermochromic Radiative Cooling Coatings with Robust Superhydrophobicity for Energy-Efficient Buildings. *Energy Environ. Mater.* **2026**, *9*, e70278.
(27) Park, S.; Park, J. Flexible Janus Patch with Reversible Adhesion, Self-Cleaning, and Enhanced Solar Reflection for Deployable Radiative Cooling. *ACS Nano* **2026**, *20*, 9507−9515.
(28) Xu, J.; Liang, F.; Wang, Z.; Chao, X.; Gu, Y.; Li, N.; Liu, H.; Wan, J.; Zhang, X.; Li, B.; Zhao, D.; Shou, D. A Durable, Breathable, and Weather-Adaptive Coating Driven by Particle Self-Assembly for Radiative Cooling and Energy Harvesting. *Nano Energy* **2024**, *124*, 109489.
(29) Wang, S.; Wu, Y.; Pu, M.; Xu, M.; Zhang, R.; Yu, T.; Li, X.; Ma, X.; Su, Y.; Tai, H.; Guo, Y.; Luo, X. A Versatile Strategy for Concurrent Passive Daytime Radiative Cooling and Sustainable Energy Harvesting. *Small* **2024**, *20*, 2305706.
(30) Cai, H.; Feng, M.; Feng, S.; He, X.; Tong, C.; Feng, D.; Liang, S.; Zhou, Y. Synchronizing Spectrum-Modulated Radiative Cooling and Integrated Heating in Hierarchical Film for All-Season Thermal Management. *Compos. Part B Eng.* **2026**, *313*, 113400.
(31) Ly, K. C. S.; Liu, X.; Song, X.; Xiao, C.; Wang, P.; Zhou, H.; Fan, T. A Dual-Mode Infrared Asymmetric Photonic Structure for All-Season Passive Radiative Cooling and Heating. *Adv. Funct. Mater.* **2022**, *32*, 2203789.
(32) Yu, H.; Yin, K.; Li, X.; Huang, Y.; Wu, T.; Xiao, J.; Wang, L.; Makarov, S. Dual-Mode Year-Round Efficient Thermal Management Using Radiative Cooling and Laser-Induced Graphene Heating. *Chem. Eng. J.* **2025**, *523*, 168794.
(33) Liu, T.; Peng, Y.; Liu, H.; Dong, J.; Long, J.; Zhang, N.; Gu, Y.; Xiao, S.; Liu, T.; Huang, Y. Janus POM/BN-Phase-Change Composite Fabric with Dynamic Radiative-Thermal-Moisture Coupling for All-Day Cooling-Heating Balance. *Chem. Eng. J.* **2026**, *535*, 175639.
(34) Fan, Q.; Fan, H.; Han, H.; Bai, Z.; Wu, X.; Hou, C.; Zhang, Q.; Li, Y.; Li, K.; Wang, H. Dynamic Thermoregulatory Textiles Woven from Scalable-Manufactured Radiative Electrochromic Fibers. *Adv. Funct. Mater.* **2024**, *34*, 2310858.
(35) Cui, T.; Zhao, Y.; Zheng, Y.; Qi, L.; Cai, W.; Wang, J.; Nie, S.; Song, W.; Hu, Y.; Yang, W.; Zhu, J. Mie-Resonant Thermochromic Safe Architectures for All-Season Radiative Thermal Management. *Adv. Energy Mater.* **2026**, *16*, No. e06717.
(36) Jin, C.; Feng, C.; Yang, J.; Huang, J.; Zhu, Y.; Lei, Y.; Feng, J.; Na, H.; Zhu, J. Nano-ITO Induced Janus Membrane Enables Spectrally Selective Photothermal Compensation for Passive Daytime Thermal Management. *Adv. Funct. Mater.* **2026**, *36*, e29459.
(37) Wang, S.; Han, H.; Du, R.; Jing, Y.; Xu, L.; Wu, S.; Li, T. Self-Adaptive Radiative Cooling/Heating Film with Energy Storage for All-Season Smart Thermoregulation. *ACS Energy Lett.* **2026**, *11*, 4343.
(38) Hu, X.; Quan, B.; Shi, Z.; Zhao, X.; Lu, G.; Ding, Y.; Lai, J.; Qu, J.; Peng, Y.; Lu, X. Bioinspired Hierarchical Radiative-Phase Change Hybrid Cooling Composite with Record-Breaking Cooling Power. *Adv. Mater.* **2026**, *38*, e10988.
(39) Mo, C.; Lei, X.; Tang, X.; Wang, M.; Kang, E.-T.; Xu, L.; Zhang, K. Nanoengineering Natural Leather for Dynamic Thermal Management and Electromagnetic Interference Shielding. *Small* **2023**, *19*, 2303368.
(40) Li, B.; Valenzuela, C.; Liu, Y.; Zhang, X.; Yang, Y.; Chen, Y.; Wang, L.; Feng, W. Free-Standing Bacterial Cellulose-Templated Radiative Cooling Liquid Crystal Films with Self-Adaptive Solar Transmittance Modulation. *Adv. Funct. Mater.* **2024**, *34*, 2402124.
(41) He, J.; Chen, Y.; Guo, R.; Tang, S. Bioinspired Colored Films with Humidity-Induced Dynamic Reflectivity and Emissivity for Self-Adaptive, Efficient Radiative Cooling. *ACS Nano* **2025**, *19*, 30361−30370.
(42) Jung, Y.; Jeong, S.; Heo, G.; Pyun, K. R.; Choi, S. H.; Bang, J.; Lee, J. G.; Kim, H.; Shin, J.; Hong, S.; Lee, J.; Won, D.; Song, J.; Ko, S. H. Monolithic Integration of Radiative Cooling and Solar Heating Functionalities by Laser-Induced Pyrolysis. *Joule* **2025**, *9*, 102007.
(43) Jin, S.; Xie, T.; Hou, J.; Mao, J.; Zhao, C.; Zhang, K.; Xiao, M.; Wang, B. Electrochemically Driven Thermal Regulation Device for Dynamic Switching between Daytime Radiative Cooling and Solar Heating with Large Solar Modulation Contrast. *Nano Lett.* **2026**, *26*, 1954−1963.
(44) Liu, W.; Dong, Y.; Li, M.; Liu, H.; Wang, X. Weather-Adaptive Janus Aerogel Integrated with Phase Change Materials Enables Dual-Mode Thermal Regulation via Radiative Cooling and Solar Heating. *Adv. Funct. Mater.* **2026**, *36*, e13665.
(45) Shi, N. N.; Tsai, C.-C.; Camino, F.; Bernard, G. D.; Yu, N.; Wehner, R. Keeping Cool: Enhanced Optical Reflection and Radiative Heat Dissipation in Saharan Silver Ants. *Science* **2015**, *349*, 298−301.
(46) Tian, Y.; Shao, H.; Liu, X.; Chen, F.; Li, Y.; Tang, C.; Zheng, Y. Superhydrophobic and Recyclable Cellulose-Fiber-Based Composites for High-Efficiency Passive Radiative Cooling. *ACS Appl. Mater. Interfaces* **2021**, *13*, 22521−22530.
(47) Wu, J.; He, J.; Yin, K.; Zhu, Z.; Xiao, S.; Wu, Z.; Duan, J.-A. Robust Hierarchical Porous PTFE Film Fabricated via Femtosecond Laser for Self-Cleaning Passive Cooling. *Nano Lett.* **2021**, *21*, 4209−4216.
(48) Zhao, Z.; Tang, C.; Cui, E.; Sun, N.; Zhou, J.; Lv, J.; Zhao, L.; Liu, Y.; Feng, S. Triple-Scale Structure-Induced Efficient Passive Radiative Cooling Combining Robust Anticondensation. *ACS Nano* **2025**, *19*, 19384−19393.
(49) Wu, X.; Li, J.; Xie, F.; Wu, X.-E.; Zhao, S.; Jiang, Q.; Zhang, S.; Wang, B.; Li, Y.; Gao, D.; et al. A Dual-Selective Thermal Emitter with Enhanced Subambient Radiative Cooling Performance. *Nat. Commun.* **2024**, *15*, 815.
(50) Sun, S.-W.; Xue, C.; Zhang, S.; Liu, M.; Zhao, J.; Li, G.; Zhang, Y.; Feng, P.; Luo, Y.-H. Combination of Radiative and Evaporative Cooling in Porous Coating Gel to Achieve High-Performance Hybrid Passive Cooling for Buildings. *Nano Lett.* **2026**, *26*, 4306−4313.